

pubs.acs.org/chemneuro Research Article

Ex Vivo Electrochemical Monitoring of Cholinergic Signaling in the Mouse Colon Using an Enzyme-Based Biosensor

Skye Henderson, Madison Strait, Roxanne Fernandes, Hui Xu, James J. Galligan,* and Greg M. Swain*



Cite This: ACS Chem. Neurosci. 2023, 14, 3460-3471



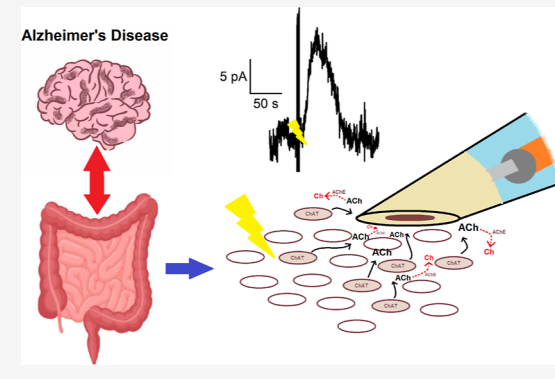
ACCESS

III Metrics & More

Article Recommendations

s Supporting Information

ABSTRACT: Cholinergic signaling, i.e., neurotransmission mediated by acetylcholine, is involved in a host of physiological processes, including learning and memory. Cholinergic dysfunction is commonly associated with neurodegenerative diseases, including Alzheimer's disease. In the gut, acetylcholine acts as an excitatory neuromuscular signaler to mediate smooth muscle contraction, which facilitates peristaltic propulsion. Gastrointestinal dysfunction has also been associated with Alzheimer's disease. This research focuses on the preparation of an electrochemical enzyme-based biosensor to monitor cholinergic signaling in the gut and its application for measuring electrically stimulated acetylcholine release in the mouse colon ex vivo. The biosensors were prepared by platinizing Pt microelectrodes through potential cycling in a potassium hexachloroplatinate (IV) solution to roughen the electrode surface and improve adhesion of the multienzyme film. These



electrodes were then modified with a permselective poly(m-phenylenediamine) polymer film, which blocks electroactive interferents from reaching the underlying substrate while remaining permeable to small molecules like H_2O_2 . A multienzyme film containing choline oxidase and acetylcholinesterase was then drop-cast on these modified electrodes. The sensor responds to acetylcholine and choline through the enzymatic production of H_2O_2 , which is electrochemically oxidized to produce an increase in current with increasing acetylcholine or choline concentration. Important figures of merit include a sensitivity of 190 \pm 10 mA mol⁻¹ L cm⁻², a limit of detection of 0.8 μ mol L⁻¹, and a batch reproducibility of 6.1% relative standard deviation at room temperature. These sensors were used to detect electrically stimulated acetylcholine release from mouse myenteric ganglia in the presence and absence of tetrodotoxin and neostigmine, an acetylcholinesterase inhibitor.

KEYWORDS: platinum microelectrodes, acetylcholine, gastrointestinal tract, enzymatic biosensor

■ INTRODUCTION

Alzheimer's disease (AD) is the most common cause of dementia and is hallmarked by the presence of extracellular amyloid beta $(A\beta)$ plaques and intracellular Tau protein tangles. Age is the number one risk factor for developing lateonset AD, though genetics and family history also play a role. For example, those carrying one or two copies of the e4 form of the APOE gene have about a 3-fold and 8- to 12-fold greater risk, respectively, of developing AD compared to those who have two copies of the e3 form of the gene. Having the e4 form of the gene, though, does not guarantee AD development.² Due to the complexity of the disease and the lack of animal models that fully mimic disease progression in humans, the early-stage pathogenesis of AD remains unclear. Although there are many hypotheses surrounding the pathogenesis of AD (i.e., the A β hypothesis, the Tau protein hypothesis, the neuroinflammation hypothesis, etc.), it is well-established that cholinergic signaling plays a vital role. The cholinergic hypothesis suggests that dysfunction of acetylcholine (ACh)containing neurons in the brain contributes to cognitive decline in those with advanced AD.3 The cholinergic

abnormalities that manifest in aged humans and AD patients include alterations in choline (Ch) transport, ACh release, and nicotinic and muscarinic receptor expression. Most current approved therapies for AD target the cholinergic system such as acetylcholinesterase (AChE) inhibitors like donepezil, rivastigmine, and galantamine. These drugs help slow (but not prevent) cognitive decline in patients with mild to moderate dementia. The cholinergic hypothesis has been around for 40+ years and—though not without flaws—portrays a convincing role for cholinergic dysfunction in AD progression. ACh is a common neurotransmitter found in both the central and peripheral nervous systems that plays a critical role in cognition, learning, memory, and neural plasticity. Utihin the periphery, ACh is the primary

Received: May 16, 2023 Accepted: August 17, 2023 Published: September 8, 2023





excitatory neurotransmitter in the enteric nervous system (ENS), mediating smooth muscle contraction to aid in the peristaltic propulsion of food content through the gastro-intestinal (GI) tract. ¹¹

The focus on neurodegenerative disease is typically dominated by the study of central nervous system (CNS) dysfunction, but there have been an increasing number of studies that indicate the involvement of the gut in early-stage AD pathology. For example, enteric AD-related protein deposition, changes in neuromuscular transmission, impaired gut function, and gut dysbiosis have been found in various AD rodent models, in some cases before full brain pathology occurs. 12-15 Cholinergic neuron loss in the brain is a prominent feature of AD pathology,5 though it is unclear whether cholinergic signaling is also affected in the ENS in AD. One study in which $A\beta$ was injected into the GI tract of a general-purpose strain of ICR mice found that $A\beta$ became internalized into cholinergic neurons in the myenteric plexus. 16 The loss of cholinergic neurons in the ileum of APP/PS1 transgenic mice has been reported¹² as well as decreased AChE activity in the small intestine of 5xFAD mice¹⁴ and reduced neurogenic cholinergic contractions in the colon of SAMP8 mice. 13 Cholinergic signaling is critical for the regulation of GI motility. Mice with conditionally deleted choline acetyltransferase (ChAT), the enzyme responsible for ACh synthesis, in neural crest-derived enteric neurons experienced dysmotility, significantly decreased colonic transit, and intestinal dysbiosis.¹⁷ Our group is interested in using electrochemical and pharmacological tools to determine if cholinergic signaling is impaired in the ENS in AD like it is in the CNS.

Electrochemical tools have long been useful in neurochemical analysis. Voltammetric and amperometric techniques which employ microelectrode or nanoelectrode sensors offer a means to detect the real-time release of electroactive signaling molecules like dopamine (DA) and serotonin (5-HT) near sites of release. However, it is often the case that the neurotransmitter of interest, such as ACh, is not electroactive and cannot be electrochemically detected directly. In cases such as this, enzymatic biosensors are often employed. Enzyme-based sensors rely on the formation of electroactive products, commonly H₂O₂, to detect these non-electroactive species. Construction of enzyme-based sensors for ACh typically involves the cross-linking of AChE and choline oxidase (ChOx) with bovine serum albumin (BSA) using glutaraldehyde on a solid support. Using this reaction scheme, ACh is hydrolyzed in the presence of AChE to produce Ch, which can then be oxidized in the presence of ChOx to produce H₂O₂ that is oxidized at the electrode interface. Crosslinking is typically done using moderate concentrations of glutaraldehyde to prevent excessive cross-linking, which can impact the enzyme's catalytic activity. 18-20 Other methods of enzyme immobilization include physical entrapment within a three-dimensional matrix such as a polymer or sol-gel, adsorption through electrostatic interaction, covalent coupling directly to a solid support, affinity bonds between functional groups on the solid support, and affinity tags within a protein sequence. 21-23 Although there are advantages and disadvantages to each method, cross-linking is typically the method of choice in the construction of ACh/Ch biosensors. 19,20,24-2

Some researchers compared enzyme immobilization through cross-linking the AChE/ChOx enzyme film on a polypyrrole-polyvinylsulpfonate modified Pt electrode vs entrapping the enzymes within the polymer film. ¹⁹ The authors found that

biosensors prepared using cross-linking with glutaraldehyde and BSA exhibit a higher affinity of the enzymes toward the electrode substrate and better operational stability. ¹⁹ Other researchers have used the self-assembly of gold nanoparticles along with AChE bound on the surface of a multi-walled carbon nanotube (MWCNT)/ChOx/sol—gel-modified Pt electrode for ACh detecion. ²⁸ Pyrolytic graphite electrodes have also been modified with MWCNTs and zinc oxide nanoparticles before depositing the dual-enzyme layer and capping the electrode with a cationic poly(diallyldimethyl ammonium chloride) polymer film to prevent enzyme leaching for Ch and ACh biosensors. ²⁷ These sensors showed excellent enzyme bioactivity as well as improved electrocatalytic activity from the MWCNTs toward $\rm H_2O_2$. ²⁷

Metal and metal oxide nanostructures (nanoparticles, nanotubes, nanorods, nanosheets, etc.) have a history of being incorporated into biosensor design and can either be coimmobilized with the enzymes or incorporated into the electrode surface. 29,30 These nanomaterials function to increase the electrochemically active surface area (ECSA), enhance the rate of electron transfer, catalyze specific chemical reactions, improve enzyme stability, or impart desired electrostatic properties during enzyme immobilization and biosensing.^{29,30} Pt metal is unique in its ability to catalyze the decomposition of H₂O₂.²⁹ Although unmodified Pt microelectrodes possess catalytic activity toward H2O2 oxidation, the incorporation of Pt nanoparticles dramatically increases the usable surface area and, consequently, the number of electrocatalytic sites.² Incorporation of Pt nanoparticles on the transducer surface has also been shown to improve the long-term stability of electrodes, improve the signal-to-noise ratio, and increase enzyme loading. $^{31-33}$

Another important consideration with the the preparation of electrochemical biosensors is selectivity. Non-conducting polymers of phenylenediamine (PD) are commonly used to enhance selectivity by allowing small molecules like $\rm H_2O_2$ to permeate through the polymer while restricting the permeability of larger molecules such as ascorbic acid (AA). 34,36,37 Thin films of this polymer with rapid response times can easily be electropolymerized in aqueous solution either before or after enzyme immobilization from the following PD isomers: o-phenylenediamine (oPD), o-phenylenediamine (oPD), and o-phenylenediamine (oPD). o-Phenylenediamine (oPD) monomer offer the best permselectivity for o-PD over o-PD monomer offer the best permselectivity for o-PD over o-PD monomer offer the oscillation of o-PD williams of o-PD over o-PD monomer offer the oscillation of o-PD over o-PD monomer offer the oscillation of o-PD over o-PD monomer offer the oscillation of o-PD over o-PD over o-PD monomer offer the oscillation of o-PD over o-PD

In this paper, we report on the use of an electrochemical biosensor and continuous amperometry (CA) to study the real-time release of ACh from myenteric ganglia in the mouse colon. We have previously developed a modified boron-doped diamond microelectrode to electrochemically monitor nitric oxide release from the mouse colon.³⁸ For this work, we prepared enzyme-based ACh/Ch biosensors based on the literature²⁴ to measure cholinergic signaling from the mouse colon in male and female wild type mice. This work is foundational for the planned use of the biosensor to study cholinergic signaling in mouse models of AD. These sensors consist of a platinized-Pt microelectrode electrodeposited with a permselective pmPD nonconductive polymer film and coated with a multienzyme film containing AChE and ChOx. ACh and Ch are detected through the enzymatic production of H_2O_2 from the reduction of the co-factor O_2 , which is electrochemically oxidized.

RESULTS AND DISCUSSION

Preparation of the Electrochemical Biosensor. The general design of the ACh/Ch biosensor is seen in Figure 1.

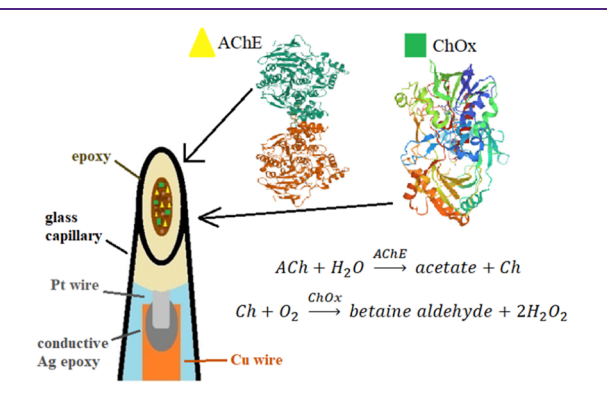


Figure 1. ACh/Ch electrochemical biosensor design and reaction scheme. Image created using protein structures from the RCSB PDB (rcsb.org) of PDB ID 1EEA³⁵ and 2JBV.⁴⁰

The microelectrode, which reveals an elliptical area of platinized-Pt, is insulated with non-conductive epoxy. Following electrodeposition of the pmPD film, a multi-enzyme film was applied to the polymer-modified electrode. As ACh is not electrochemically active, ACh is indirectly measured through the oxidation of enzymatically produced $\rm H_2O_2$. Briefly, ACh is hydrolyzed in the presence of AChE to produce Ch. In turn, Ch is then oxidized in the presence of the second enzyme, ChOx, to produce 2 mol of $\rm H_2O_2$ using the co-factor, $\rm O_2$. The $\rm H_2O_2$ diffuses through the porous pmPD film to be oxidized at the platinized-Pt interface, generating a current response that is directly proportional to ACh concentration. The sensor also responds to Ch via the second enzymatic reaction only.

To enhance the electrochemically active area of the electrode and to "roughen" the substrate for better enzyme adhesion, Pt nanoparticles were electrodeposited onto the microelectrodes prior to pmPD electrodeposition and enzyme immobilization. Cyclic voltammograms showing the electrodeposition of Pt nanoparticles and the change in ECSA before and after electrodeposition can be seen in Figure 2. In Figure 2A, one can see the reduction of Pt(IV) to Pt metal on the first potential sweep with an increase in cathodic current starting at ~0.05 V, initiating nucleation. With increasing cycle number, there is an increase in oxidation current at ~1.0 V for Pt-oxide formation, an increase in cathodic current at ~0.6 V for Ptoxide reduction, and an increase in voltammetric current between 0.1 and -0.2 for hydrogen adsorption and desorption as more Pt nanoparticles form and grow out from those nucleation sites. In Figure 2B, the same electrode is potential cycled in 0.5 mol L-1 H₂SO₄ before and after electrodeposition. A significant increase in the ECSA of the electrode is evident, with a hydrogen desorption charge increase from 21.0 nC to 559 nC, producing a roughness factor of 37.

The pmPD films were prepared by potential cycling the platinized-Pt microelectrodes in a solution containing 5 mM mPD monomer in 0.1 mol L^{-1} phosphate buffer (PB), pH 7.4. A sample cyclic voltammogram illustrating this process can be seen in Figure 3. As potential is swept from 0.2 to 1.0 V, there is a large oxidation peak that occurs around 0.6 V in which the mPD monomer is oxidized to produce a radical cation. These radical cations are very reactive and couple with one another to produce dimers, which are more easily oxidized due to more

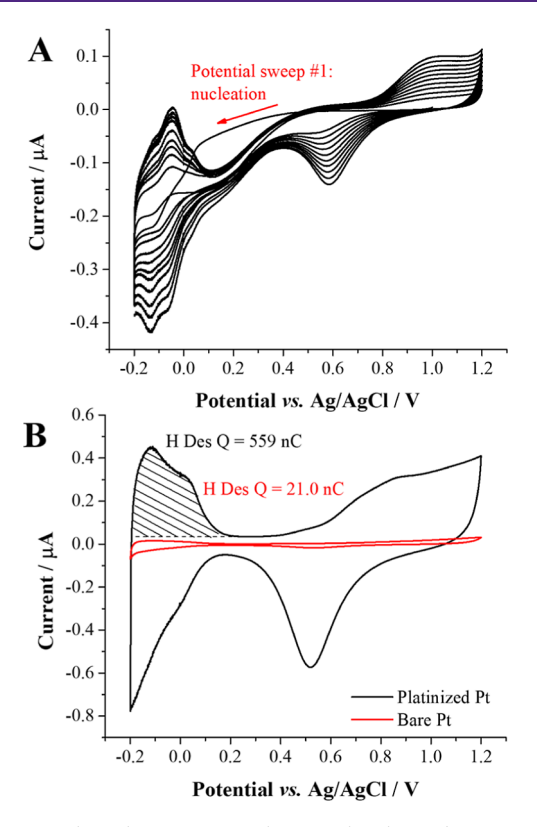


Figure 2. Cyclic voltammograms showing the electrodeposition of Pt nanoparticles by potential cycling a deoxygenated 2 mmol L^{-1} $\rm K_2PtCl_6$ solution from -0.2 to 1.2 V at 10 mV s $^{-1}$ for 10 cycles with the first cathodic sweep starting at 1.0 V (A). Cyclic voltammogram showing the same electrode shown in (A) before and after electrodeposition in 0.5 mol L^{-1} sulfuric acid (B). The last of 8 cycles is shown at 50 mV s $^{-1}$.

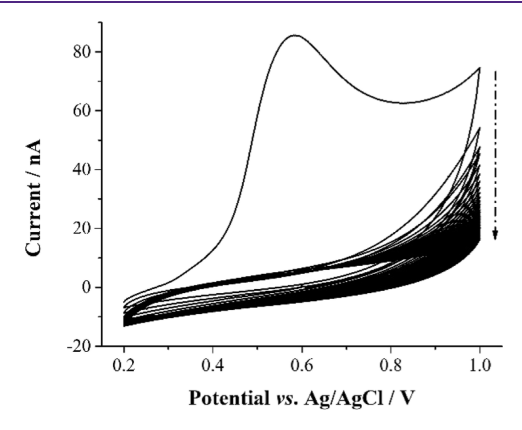


Figure 3. Cyclic voltammograms showing the electrodeposition of the pmPD films prepared by potential cycling the platinized-Pt microelectrodes in a solution containing 5 mM mPD monomer in 0.1 mol $\rm L^{-1}$ PB, pH 7.4. A large oxidation peak for mPD oxidation at ~0.6 V is evident that disappears with increasing cycle number as the self-passivating pmPD coats the entirety of the electrode. The oxidation charge for this peak is 186 nC.

extensive π electron delocalization, increasing the electron density around the redox sites. ^{37,41} As those dimers become oxidized, the chain length grows, and the branched pmPD film forms. ⁴¹ The oxidation charge for this peak is 186 nC. With increasing cycle number, this oxidation peak disappears as the self-passivating pmPD film insulates the electrode and prevents further monomer oxidation, forming a thin, uniform coating

across the electrode substrate. The optimization of the electrodeposition scan rate and cycle number can be seen in Figure S1.

Following pmPD electrodeposition, 1 μ L of a multienzyme solution consisting of equal parts of 200 U mL⁻¹ ChOx, 400 U mL⁻¹ AChE, 10% (w/v) BSA for enzyme stabilization, and 0.75% (v/v) glutaraldehyde was deposited onto the modified electrodes, dried for 2 h at room temperature bbefore immersing in 0.1 mol L⁻¹ PB, pH 7.4, and storing at 4 °C. The volume of this multienzyme solution was optimized for peak response to ACh (see Figure S2).

Pt Nanoparticle and pmPD Film Morphology. Prior to pmPD electrodeposition, Pt microelectrodes were roughened by electrodepositing Pt nanoparticles using cyclic voltammetry (CV) in a 2 mmol L⁻¹ K₂PtCl₆ solution. This modification not only enhanced the sensitivity of the biosensors, but it also improved batch reproducibility (see Figure S3). One can see the change in the microelectrode's morphology at each step of the electrode fabrication process in Figure S4, which presents scanning electron microscopy (SEM) micrographs in the secondary electron image mode. A bare Pt substrate can be seen in Figure S4A. The surface is relatively smooth with the exception of long striations introduced during the metal wire formation. Figure S4B shows the platinized-Pt substrate, which exhibits a highly roughened surface decorated by small and large Pt nanoparticles. Figure S4C shows the same platinized-Pt microelectrode at a lower magnification, revealing the Pt nanoparticle coverage conforming to the ridges in the Pt substrate. Figure S4D shows a platinized-Pt microelectrode coated with the pmPD polymer film. One can see a thin film that bridges the Pt nanoparticles together, but it is difficult to discern the polymer morphology.

To better visualize the films and discriminate between the polymer coating and Pt, a bare Pt wire (80 µm diam.) was partially coated in pmPD by immersion into a deoxygenated 5 mmol L⁻¹ mPD in 0.1 mol L⁻¹ PB, pH 7.4, solution and scanning from 0.2 to 1.0 V at 25 mV s⁻¹ for 40 cycles. Figure 4 presents SEM micrographs of this pmPD film. In Figure 4A, one can delineate the polymer-coated and uncoated regions of the Pt wire. In Figure 4B, a higher magnification micrograph of the pmPD coating reveals good polymer coverage that conforms to any roughness features on the native Pt wire. In Figure S5A, a cross section of the pmPD-coated Pt wire is seen in which a blade was used to cut through the electrode postpolymerization. The polymer film detached and flaked off the surface at the cut edge. These pieces of delaminated polymer reveal a film thickness of \sim 50 nm, which is slightly higher than what has been reported in literature 34,36,37 The polymer accumulates in roughened regions of the Pt substrate to form large and small clusters of pmPD in these areas. Figure S5B reveals a larger pmPD cluster, revealing small pores and channels that span across the polymer. This is typical of pmPD films, which tend to have a very porous morphology that allows small molecules, like H₂O₂, to partition in and diffuse through while rejecting larger molecules, like AA, DA, norepinephrine (NE), and 5-HT from reaching the underlying substrate. 34,36,37,42 Figure S5C reveals a small cluster of pmPD, which shows a distinct spherical morphology.

Electrochemical Characterization of the Biosensors. To determine the detection potential to be used for the amperometric experiments, linear sweep voltammetry (LSV) was used to determine the oxidation potential of enzymatically generated H_2O_2 . Figure 5A shows voltammograms for

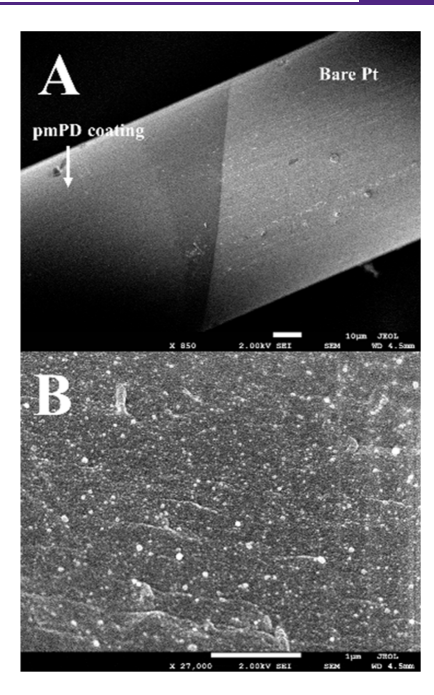


Figure 4. Secondary electron micrographs of a length of Pt wire (80 μ m diam.) that was partially coated with pmPD. Micrograph A shows the boundary between the coated and uncoated regions of the wire, and micrograph B shows a more magnified region of the pmPD-coated wire, which indicates good coverage of the polymer over the Pt substrate.

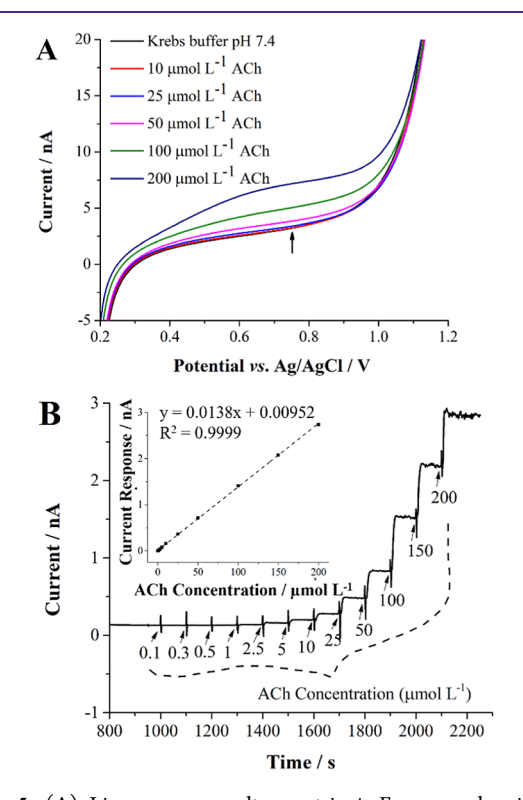


Figure 5. (A) Linear sweep voltammetric i-E curves showing the response to increasing concentrations of ACh added to Krebs buffer, pH 7.4. The scan rate was 10 mV s⁻¹. Amperometric i-t curve (B) showing an oxidation current that increases proportionally with increasing ACh concentration added to 10 mL of magnetically stirred Krebs buffer, pH 7.4. The detection potential was 0.75 V vs Ag/AgCl.

increasing concentrations of ACh added to 10 mL of Krebs buffer, pH 7.4, with the potential being swept from 0.2 to 1.2 V. The scan rate used was 10 mV s⁻¹. One can see the onset of oxidation at ~0.4 V and a significant increase in voltammetric current with increasing ACh concentration at ~0.7 V. At this potential, the current is at its maximum and mass transport limited. In data not shown, an experiment was conducted to evaluate if mass transport for this process was diffusion-limited. A series of cyclic voltammograms were collected as a function of scan rate in response to 1 mmol L⁻¹ H₂O₂. It was revealed that the peak oxidation current increases linearly with scan rate, as opposed to scan rate^{1/2}. This suggests that adsorption of H₂O₂ occurs during electrochemical oxidation. The likely explanation for this is that H₂O₂ adsorbs to Pt-oxide formation sites, electron transfer occurs between the Pt-oxide/adsorbed H₂O₂ complex, consequently reducing those surface sites, and those binding sites then become electrochemically regenerated, giving rise to the observed current response. 43,44 For multiple ACh/Ch biosensors, E_p^{ox} was 0.67 \pm 0.05 V (n = 5). Based on the voltammetric data, a detection potential of 0.75 V was selected for the CA experiments. Figure 5B shows an example amperometric i-t curve in which a biosensor was polarized at 0.75 V and an increasing concentration of ACh was added every 100 s to 10 mL of magnetically stirred Krebs buffer at room temperature. The biosensor responds rapidly in the amperometric detection mode to the ACh additions, producing an increase in oxidation current that responds linearly from 0.5 to 200 μ mol L⁻¹, as is evident in the response curve inset.

Determination of Detection Figures of Merit. Based on the detection scheme in Figure 1, the biosensor responds to both Ch and ACh. It is possible to detect ACh only if two separate sensors are prepared: one with AChE and ChOx immobilized and the other with only ChOx immobilized. By employing both sensors in the sensing media and subtracting the ChOx-only response, changes in basal levels of ACh can be determined.²⁴ However, this can become difficult in practice due to variability in electrode fabrication. Some researchers have overcome this by producing mass-fabricated microelectrode arrays which are much more uniform in design and manufacture. However, these recording sites are 100 μ m from one another, limiting spatial resolution.²⁶ Due to the nature of our measurements and their dependence on electrode position on current response, it is not possible to employ a similar electrode for our measurements. As ACh is rapidly hydrolyzed into Ch by AChE following synaptic release, ex vivo measurements are a combination of ACh and Ch release and a tool for measuring cholinergic neuronal function rather than isolating the ACh response specifically. Figure 6 shows example i-t curves showing the difference in sensor response to Ch versus ACh (A) and how the response to equimolar additions of ACh compares to equimolar additions of the electroactive interferents AA, DA, NE, and 5-HT (B). In both curves, the electrode was polarized at 0.75 V versus Ag/AgCl, and the electrolyte was 10 mL of magnetically stirred Krebs buffer, pH 7.4. The current responses to Ch and ACh are nearly identical for n = 3sensors (p = 0.76), as is the response time (p = 0.99), suggesting that the conversion of ACh to Ch occurs rapidly. The biosensor responds reproducibly to both Ch and ACh with repeat 10 μ mol L⁻¹ additions of each, with a RSD of 4.7% for Ch and 0.7% for ACh for n = 5 additions. One can see that although the biosensor responds reproducibility to ACh, there

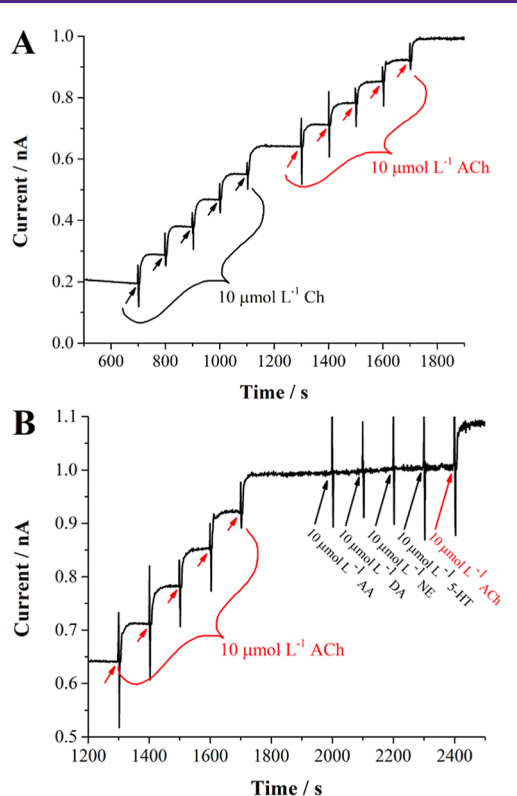


Figure 6. Amperometric i-t curves (A) showing the respective responses to equimolar additions of Ch and ACh added to 10 mL of magnetically stirred Krebs buffer, pH 7.4. The detection potential was 0.75 V vs Ag/AgCl. A second amperometric i-t curve (B) showing the response to equimolar additions of ACh followed by equimolar additions of electroactive interferents AA, DA, NE, and 5-HT. The last addition returns to ACh. Both measurements were made at room temperature.

is little to no response to the equimolar additions of AA, DA, NE, and 5-HT. This indicates excellent selectivity toward ACh and Ch, making the biosensor useful for measuring cholinergic signaling in complex media.

Table 1 summarizes the detection figures of merit calculated for the biosensors to ACh from CA measurements made at room temperature. The sensitivity is normalized to the geometric area of the microelectrode. The response time was defined as the time it took for the current response to 50 μ mol L⁻¹ ACh to rise from 5 to 90% of its maximum steady state response. The response time is competitive with other ACh/ Ch biosensors, which are typically $\geq 8 \text{ s}^{18,19,27,28}$ but slower than other biosensors utilizing pmPD, which are typically ≤ 1 s.²⁴⁻²⁶ This is likely because our pmPD films appear to be thicker than what is typically observed in the literature, which is 10-35 nm. 34,36,37 Although there seems to be little effect on sensitivity, our thicker pmPD films (\sim 50 nm) are likely slowing response time. The reproducibility was determined by calculating the RSD of the slope of the response curves within a single batch of biosensors (n = 3). The selectivity ratio for AA, DA, NE, and 5-HT was determined from the current response to ACh normalized to the current response of each interferent. The lifetime of the biosensors was assessed by preparing a batch of biosensors and using CA to determine the current response from 0.5 to 100 μ mol L⁻¹ ACh at room temperature immediately after biosensor preparation, after 7 days of storage, and after 14 days of storage. The electrodes

Table 1. Detection Figures of Merit for ACha

sensitivity (mA mol ⁻¹ L cm ⁻²)	190 ± 10
LOD (μ mol L ⁻¹)	0.8 ± 0.3
$LOQ (\mu mol L^{-1})$	2.9 ± 1.0
linear dynamic range (μ mol L ⁻¹)	3-130
response time (s)	2 ± 1
reproducibility	6.1% RSD
selectivity $I_{\rm ACh}/I_{\rm interferent}$	125 ± 1 (AA), 60 ± 1 (DA), 24 ± 1 (NE), 50 ± 1 (5-HT)
lifetime	≥2 weeks

"Values are the average \pm standard deviation (SD) for n=3 electrodes for measurements conducted at room temperature (25 °C). The limit of detection (LOD) is defined as $S/N \ge 3$, and the limit of quantification (LOQ) is defined as $S/N \ge 10$.

were stored immersed in 0.1 mol L^{-1} PB, pH 7.4, in the refrigerator at 4 °C between measurements. The average biosensor response for n=3 sensors was recorded. The respective response curves can be seen in Figure S6. Over a two-week period, there was no change in sensitivity for the three biosensors. Therefore, for ex vivo measurements, the sensors were used within two weeks of preparation.

Ex Vivo Electrochemical Measurements. To prepare for ex vivo measurements, the effects of oxygenation and physiological temperature were evaluated. Similar to the experimental setup used for the tissue measurements, Krebs buffer, pH 7.4, was perfused through a recording chamber at 4 mL min⁻¹, while the working electrode was positioned at the center of the chamber using a micromanipulator. The electrode was polarized at 0.75 V versus Ag/AgCl, and the background current was allowed to stabilize. Using standard solutions, 1, 3, 5, and 10 μ mol L⁻¹ ACh were perfused through the recording chamber with a brief rinse period between each concentration. For a single biosensor, these measurements were performed at room temperature (25 °C), after bubbling O2 gas into the buffer for 20 min prior to and during the measurement, and at physiological temperature (37 °C) with oxygenation. The data can be seen in Figure 7. There is not a significant difference in the response after oxygenation, indicating that atmospheric O₂ provides a sufficient concentration of the cofactor needed for Ch oxidation in the enzymatic reactions. Unsurprisingly, increasing the temperature nearly doubled the sensitivity of the sensor.

To account for sensor-to-sensor variability during the ex vivo measurements, a calibration was performed prior to each tissue measurement in the flow bath. A sample i-t curve and its corresponding response curve can be seen in Figure 8 in which warmed (36-37 °C) Krebs buffer, pH 7.4, was perfused through a recording chamber at 4 mL min⁻¹. The electrode was polarized at 0.75 V versus Ag/AgCl, and increasing concentrations of ACh were perfused through the chamber after the background current stabilized. A rinse was performed following the final ACh concentration, and restoration of baseline current was achieved. The sensitivity from these calibrations was used to estimate the peak concentration of ACh/Ch detected in the extracellular solution around the biosensor after electrical stimulation of nearby myenteric ganglia in the mouse colon. Compared to the measurements conducted at room temperature, the LOD decreased to 0.3 \pm 0.2 μ mol L⁻¹ and the sensitivity increased to 360 \pm 60 mA mol⁻¹ L cm⁻² for n = 6 sensors at physiological temperature.

To determine how many times a single biosensor could be used for ex vivo measurements, a calibration was performed using a biosensor over four consecutive days, running a full tissue measurement after each calibration. These data can be

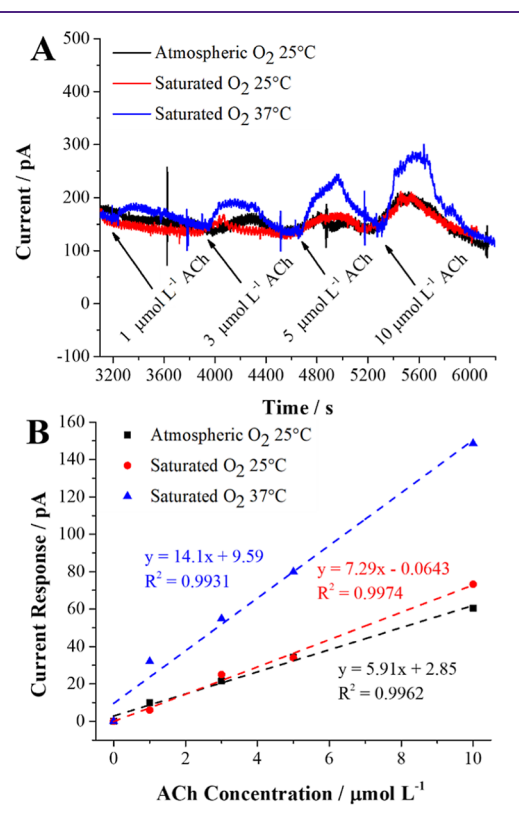


Figure 7. Amperometric i-t traces (A) showing the biosensor's response to increasing concentrations of ACh added to Krebs buffer pH 7.4, which is continuously perfused through a recording chamber at 4 mL min⁻¹. A brief rinse period with buffer was performed between additions. The detection potential was 0.75 V vs Ag/AgCl. The respective response curves can be seen in (B), where the black trace shows the current response at room temperature (25 °C), the red trace shows the current response at room temperature but after saturating the buffer with O_2 , and the blue trace shows the current response after oxygenating the buffer and increasing the temperature to physiological temperature (37 °C).

seen in Figure S7. There is little loss in sensitivity between days 1 and 2, less than 5%. However, after day 3, the sensitivity decreases by 30% and by day 4, it decreases by 57%. This gradual decline with prolonged use ex vivo is not that surprising, as proteins in the tissue can progressively adsorb to the electrode surface, fouling the substrate. Therefore, individual biosensors were not used for more than two ex vivo measurements. For experiments in which two animals were tested within the same day, the same sensor was used, but with a brief second calibration performed in response to 1 μ mol L⁻¹ ACh additions to ensure that the same current response was achieved.

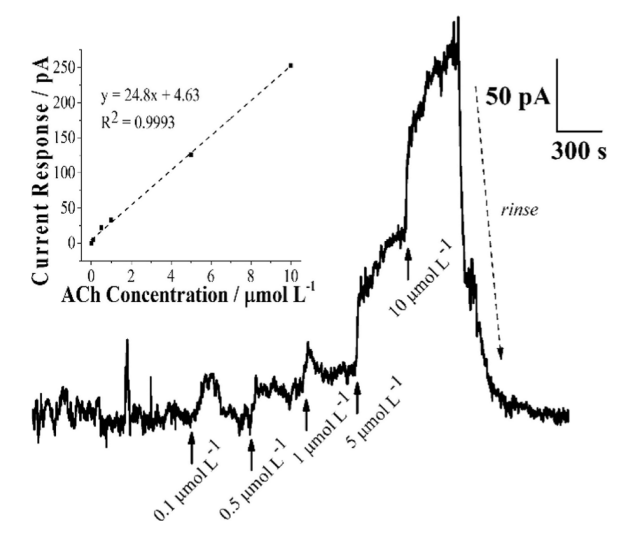


Figure 8. Continuous amperometric i–t curve and corresponding response curve (inset) showing the calibration of a single biosensor using standard ACh solutions prior to an ex vivo measurement. The detection potential was 0.75 V vs Ag/AgCl, and the electrolyte was Krebs buffer, pH 7.4, perfused at 4 mL min⁻¹ at 37 °C. The current was smoothed by a 10 Hz lowpass filter.

For ex vivo measurements, the number of electrical stimuli delivered to the tissue was gradually increased, and the corresponding current response was recorded. The measured current response results from a combination of synaptic ACh release and Ach, which has been hydrolyzed into Ch by ACh in the extracellular space. Due to time limitations, replicate stimulations were not performed for each set of electrical stimuli, but we did verify that identical stimulations produced identical current responses. This data is presented in Figure S8. Figure 9 shows a sample response for a single male and female mouse in which the tissue is stimulated for 10, 20, 30, 40, and 50 pulses at 10 Hz, 80 V, 0.5 ms pulse duration. Stimulations were performed every 5–10 min, allowing sufficient time for vesicular restoration to occur^{45,46} The *i-t* traces are normalized to each electrode's calibration to display the

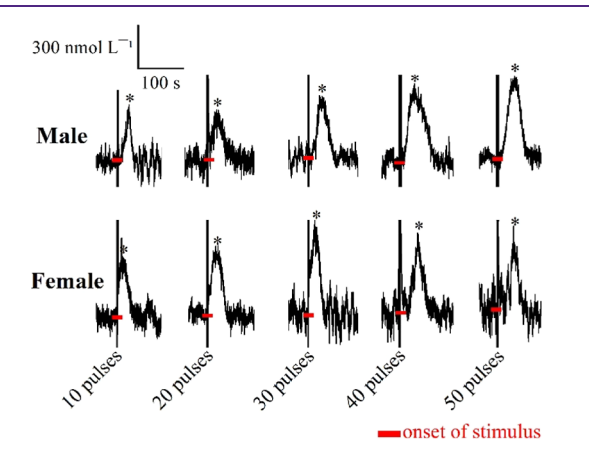


Figure 9. Ex vivo continuous amperometric responses generated by normalizing the i-t curves to their respective calibrated sensitivities show the change in extracellular concentration of ACh/Ch following 10, 20, 30, 40, and 50 electrical stimuli at 10 Hz, 80 V, and 0.5 ms pulse duration. The red bars indicate the onset of the stimulus. The detection potential was 0.75 V vs Ag/AgCl. The data was filtered through a 10 Hz lowpass filter.

extracellular ACh/Ch concentration with respect to time. A slight increase in peak ACh/Ch concentration can be seen from 10 to 40 pulses. From 40 to 50 pulses, the peak concentration is the same, but the peak broadens, indicating that at 40 pulses, the peak rate of release is obtained, but a greater number of stimuli prolongs this release. The mean \pm standard error of mean (SEM) peak concentrations as well as the integrated area of each peak can be seen in Figure 10.

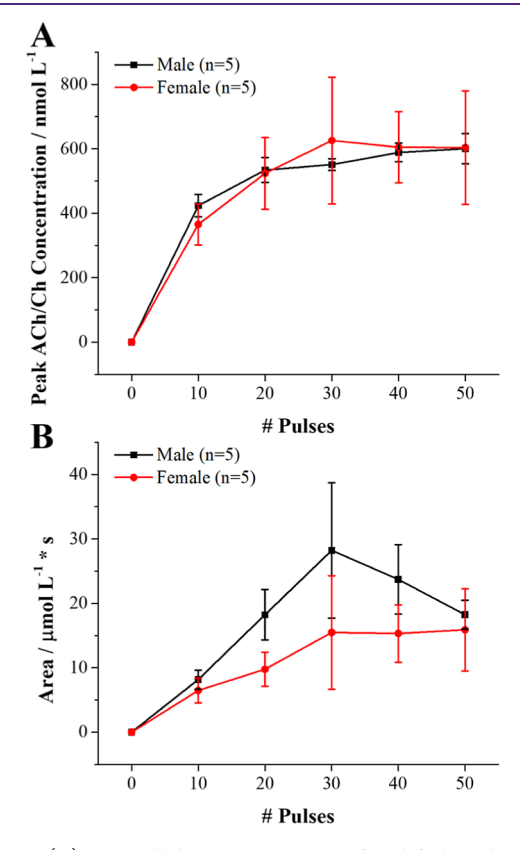


Figure 10. (A) Extracellular concentrations of ACh/Ch evoked with a tissue stimulation of 10-50 pulses at 10 Hz, 80 V, 0.5 ms pulse duration, and the corresponding integrated areas of the current responses (B). Data are presented as mean \pm SEM for n=5 male and n=5 female mice.

Overall, with the exception of the mean comparison between 10 and 40 and 10 and 50 pulses for the peak ACh/Ch concentration for the male mice, there is not a significant increase in peak concentration or area with an increasing number of electrical stimulation pulses. This suggests that these electrical stimulation conditions elicit a peak neurotransmitter release from cholinergic enteric neurons. A current response was unable to be recorded using fewer than 10 electrical stimuli, as these concentrations are likely below the LOD (0.3 \pm 0.2 μ mol L⁻¹ at physiological temperature) of the sensor. The peak concentrations of ACh/Ch detected are identical between the male and female mice. Likewise, there is not a significant sex difference when comparing the respective areas of the peaks. The peak ACh/Ch concentration for the male mice was 600 ± 47 nmol L⁻¹ at 50 pulses, and the peak concentration for the female mice was 626 ± 197 nmol L⁻¹ at 30 pulses. Due to the absence of similar studies in the gut, our results cannot be compared directly with any literature data. The amount of ACh/Ch detected will depend on the distance of the microelectrode from the release sites and the number of

cholinergic neurons in the vicinity of the microelectrode, offset by the rate of clearance. ACh concentration in the brain extracellular fluid is in the low nanomolar range 47,48 Naturally, electrically stimulated tissue would elicit a higher local ACh concentration. For example, in an ex vivo experiment, electrically stimulated mouse brain slices elicited an ACh concentration of 0.41 \pm 0.05 μ mol L⁻¹.⁴⁹ In another study, KCl and nicotine were used to stimulate ACh release from the prefrontal cortex in rats in vivo. Low micromolar levels of ACh were detected using a microelectrode array.²⁵ It is generally accepted that synaptically released ACh can reach a peak millimolar concentration at the neuromuscular junction; however, this concentration decays rapidly due to diffusion, reuptake, metabolism, and receptor binding.⁵⁰ Unless using nanoelectrodes, it is not possible to probe the synaptic cleft where ACh concentration is at its peak. Rather, we are measuring a small fraction of ACh or Ch, which has been formed through the metabolism of ACh that diffuses away from multiple cholinergic release sites. This suggests our measurements, which are in the submicromolar range, could possibly be a reasonable estimate.

In cholinergic neurons, ACh is synthesized by ChAT using Ch and acetyl-CoA. When ACh is released across a chemical synapse, it acts on nicotinic or muscarinic receptors, or, conversely, the actions of ACh are terminated by AChE, and ACh is hydrolyzed into Ch and acetate for reuptake and recycling. By inhibiting AChE with a drug like neostigmine, one can increase the time that ACh resides in the extracellular solution, consequently increasing the area of our measured current response and confirming that the source of oxidation current is in some part due to ACh.

Example continuous amperometric i-t traces showing the general pharmacological scheme that was followed for the ex vivo electrochemical measurements using a single 50 pulse stimulation can be seen in Figure 11. After completing the electrical stimulations, the tissue was perfused with 0.3 μ mol L⁻¹ TTX, and the stimulations were repeated. After perfusing

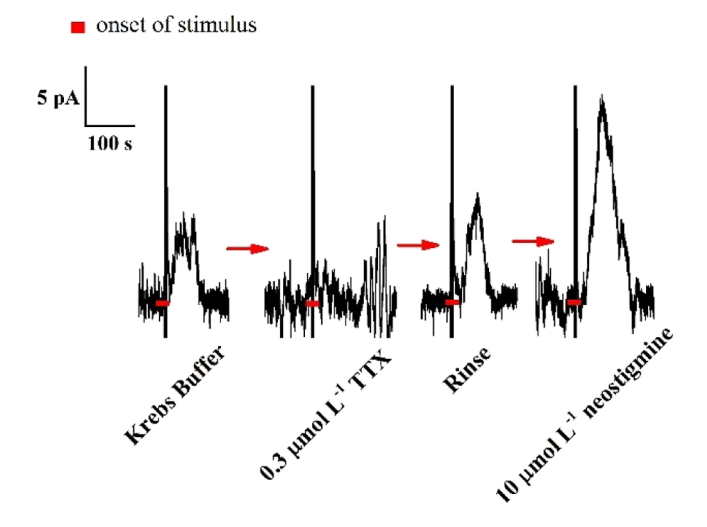


Figure 11. Sample continuous amperometric *i*—*t* curves showing the pharmacological sequence followed during ex vivo measurements. A single stimulation is shown in which 50 electrical stimuli at 10 Hz, 80 V, and 0.5 ms pulse duration are delivered to the tissue preparation. The red bars indicate the onset of the stimulus. The detection potential was 0.75 V vs Ag/AgCl. The data was filtered through a 10 Hz lowpass filter.

TTX, there is some electrical noise ~100 s downstream of the stimulation. However, one can see that the current response, which previously manifested as a sharp spike immediately following the electrical stimuli, is nearly abolished after perfusing the sodium channel blocker. This indicates that the current response is of neurogenic origin and that release occurs via an action potential-dependent process. Next, the tissue was rinsed with buffer, and a single stimulation was repeated to verify that the TTX was rinsed out, and the original current response was restored. Lastly, the tissue was perfused with 10 μ mol L⁻¹ neostigmine, an AChE inhibitor. This drug prevents the breakdown of ACh from occurring, resulting in an increase in the half-life of ACh in the synaptic cleft. This extension in time that ACh sits in the extracellular space should hypothetically prolong the action of ACh and consequently increase the local concentration of ACh and delay the breakdown into Ch, resulting in an amperometric peak with a greater area than before drug perfusion.

A summary of the drug responses for the male and female mice is presented in Figure 12, in which the area of the

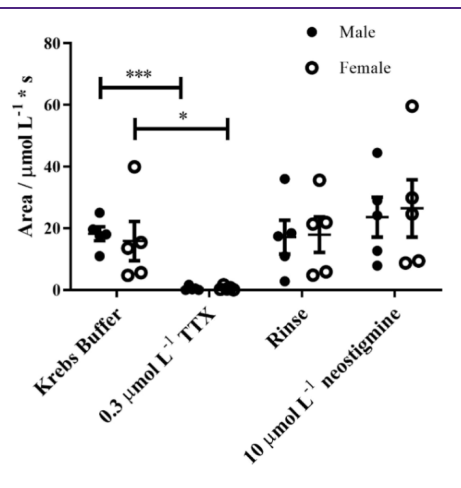


Figure 12. The mean \pm SEM integrated peak area normalized to each biosensor's calibrated sensitivity for the amperometric responses to 50 pulses of electrical stimuli at 10 Hz, 80 V, and 0.5 ms pulse duration for male (n=5) and female (n=5) control mice in the presence and absence of 0.3 μ mol L⁻¹ TTX and 10 μ mol L⁻¹ neostigmine. * $p \le 0.05$, *** $p \le 0.001$.

oxidation peak following the 50 pulse electrical stimulation is compared before and after drug application. The response is essentially abolished in the presence of TTX. The response can be seen to be completely restored after rinsing TTX out. Overall, there is only a slight, far from significant, increase in response after perfusing neostigmine, but the response was variable not only from animal to animal but also within the same animal. For example, in most cases, only the first stimulation performed after perfusing the drug resulted in an enhanced ACh response, whereas repeated stimulations were often dramatically reduced. It is possible that the concentration of the AChE inhibitor was not high enough to see the desired response or that these observations are the result of some controversial effects of AChE inhibitors. For example, it has been found that the exaggerated concentration of ACh in the extracellular space could activate inhibitory autoreceptors on the cholinergic neurons, therefore reducing the cholinergic neurons response to electrical stimulation.⁴⁸ However, the more likely explanation is that the bulk of the measured

response is from Ch formed from the hydrolysis of ACh rather than ACh itself. When using analytical techniques such as microdialysis, measured concentrations of ACh versus Ch are overwhelmingly dominated by Ch^{47} with extracellular ratios of ACh/Ch being about 1:12. On the other hand, when using techniques like electrochemical detection with rapid response times, ratios of ACh/Ch can be as close as 1:1. However, these sensors exhibit response times ≤ 1 s, so it is likely that our current sensor design does not respond fast enough to capture ACh concentration before being converted over to Ch. This is something that could be improved upon by implementing thinner films of pmPD, which provide a less tortuous path for $\mathrm{H}_2\mathrm{O}_2$ to diffuse through.

CONCLUSIONS

ACh/Ch biosensors, which are selective against AA, DA, NE, and 5-HT, were successfully prepared and applied to measure electrically stimulated ACh release from myenteric ganglia in the mouse colon. We estimated a measured peak ACh/Ch concentration of 600 ± 47 nmol L⁻¹ for the male mice and 626 $\pm~197~\text{nmol}~\text{L}^{-1}$ for the female mice. The current responses were abolished in the presence of the sodium channel blocker TTX, suggesting that the measured current response is neurogenic in origin. The current response was elevated slightly in the presence of the AChE inhibitor neostigmine, suggesting that the bulk of the current response measured is from Ch, which has been formed through the hydrolysis of ACh rather than ACh itself. This is one of the limitations of this sensor design, which is the inability to differentiate between ACh and Ch unless utilizing two separate sensors. This can be problematic, as ACh is rapidly hydrolyzed following synaptic release to Ch by AChE. Regardless, these sensors provide a useful tool for measuring cholinergic signaling that can be applied ex vivo. We plan on using these sensors to measure ACh/Ch release in an APP/PS1 mouse model of AD to determine if cholinergic signaling is also affected in the ENS of AD.

■ EXPERIMENTAL METHODS

Reagents. Most reagents, including sulfuric acid (H2SO4 99.999%, SHBK1251), potassium hexachloroplatinate (IV) (K₂PtCl₆, 98%, 05720TI), m-phenylenediamine flakes (mPD, 99%, WXBC0066V), acetylcholinesterase from Electrophorus electricus (AChE ≥1000 units/mg protein, SLCF0924), choline oxidase from Alcaligenes sp. (ChOx \geq 10 units/mg solid, SLCM2414), BSA (\geq 96%, SLCF3210), glutaraldehyde (25% in H₂O, SLBC7631V), acetycholine chloride (ACh) (≥99%, BCCD7863), choline chloride (Ch, ≥99%, BCCF5311), L-ascorbic acid (AA, ≥99.0%, SLCO4212), dopamine hydrochloride (DA, ≥98%, BCBF7218V), DL-norepinephrine hydrochloride (NE, ≥97%, MKCC1425), and serotonin hydrochloride (5-HT, ≥98%, SLCC3073), were purchased through Sigma-Aldrich (USA) and used as received. PB, pH 7.4, was prepared from sodium phosphate monobasic (NaH₂PO₄, ≥99.0%, BCCF7956) and sodium phosphate dibasic (Na $_2$ HPO $_4$, \geq 99.0%, BCCF9828). Krebs buffer, pH 7.4, containing 117 mmol L $^{-1}$ NaCl, 4.7 mmol L $^{-1}$ KCl, 2.5 mmol L⁻¹ CaCl₂, 1.2 mmol L⁻¹ MgCl₂, 1.2 mmol L⁻¹ NaH₂PO₄, 25 mmol L^{-1} NaHCO₃, and 11 mmol \tilde{L}^{-1} glucose, was prepared fresh daily. For tissue measurements, nifedipine (1 μ mol L⁻¹, 113K1408) was added to the perfusing Krebs buffer and continuously applied throughout measurements to prevent spontaneous muscle contractions. The sodium channel blocker tetrodotoxin (TTX, 0.3 μ mol L $^{-1}$ Cayman Chemical, 0650675-1, CAUTION: potent neurotoxin, use with extreme care) and AChE inhibitor neostigmine (10 μ mol L⁻¹, 83C-1180) were also continuously added to the perfusing buffer in drug experiments.

Animal Model. For animal experiments, all procedures were approved by the Institutional Animal Use and Care Committee (IACUC) at Michigan State University. Experiments were conducted on male (n = 5) and female (n = 5) control mice only of an APP/PS1 double transgenic mouse strain (B6C3-Tg(APPswe,PSEN1dE9)-85Dbo/Mmjaxries; MMRRC034829, Stock: 004462-JAX) purchased from Jackson Laboratory at 8 weeks old (https://www.jax.org/strain/ 004462) and sacrificed after 12 months. All mice were maintained on a C57BL/6; C3H (B6C3) genetic background. Although genetic control mice were used for this study, it is a future goal to use this model to explore amyloid plaque formation and neurogenic dysfunction in the GI tract. All animals were housed in a 12 h light/dark cycle with 68% humidity levels in the house, with ad libitum access to water and food (Tekla Global 18% protein diet (2918)). Euthanasia was performed in compliance with the Panel on Euthanasia of the American Veterinary Medical Association using 4% isoflurane and cervical dislocation as approved.

Instrumentation. CV, LSV, and CA experiments in a standard, single-compartment electrochemical cell were made using a computer-controlled electrochemical workstation (model 832A, CH Instruments, Austin, TX) using a Pt wire counter electrode and a commercial Ag/AgCl (3 mol L-1 KCl) reference electrode (Bioanalytical Systems Inc., West Lafayette, IN). For the ex vivo electrochemical measurements, an Omni 90 analog potentiostat (formerly Cypress Systems Inc.) was used for CA experiments, and it traces were recorded using an Axon Digidata 1400A Low-Noise Data Acquisition System with Axoscope 10.7 software (Molecular Devices, Sunnyvale, CA). Data were filtered using a 10 Hz low-pass filter and analyzed using Clampfit 10.7 software (Molecular Devices). Transmural electrical stimulation was performed by delivering voltage pulses (80 V, 10 Hz, 0.5 ms pulse duration) across two Ag/AgCl wires applied on either side of the tissue preparation using an electrically isolated Grass S88 stimulator (Grass Technologies, West Warwick,

Platinum Microelectrode Preparation. Microelectrodes were prepared by contacting one end of an 80 µm diam. Pt (Goodfellow, 99.9%) wire to a ~3 in. piece of 0.25 mm diam. Cu (Aldrich, 99.9%) wire using conductive silver epoxy and curing overnight. The next day, the Pt-Cu wires were threaded through glass capillaries (1.2 mm diam), which were pulled to a taper using a P30 vertical micropipette puller (Sutter Instruments) and cut open so that a small gap of space was present between the opening of the glass capillary and the Pt wire. This end of the microelectrode was then immersed in a two-part epoxy mixture for 30-60 s, which was prepared by mixing equal parts epoxy resin and hardener (Gorilla Clear Epoxy). Through capillary action, epoxy was drawn into the tip of the capillary to form a resin plug, insulating the electrode. The back end of the capillary was also sealed using the same epoxy. Excess epoxy was quickly wiped from the outside of the capillary using a Kimwipe, and the resin was allowed to cure overnight at room temperature. The next day, electrodes were placed in the oven for 1-2 h at 70 °C to further harden the epoxy, and the electrodes were then ground at 45° using a BV-10 micropipette beveler (Sutter Instruments) using a course diamond abrasive plate (Cat. #104C, Sutter Instruments). This exposed an elliptical disk area of the Pt wire with a geometric area of 7.1×10^{-5} cm⁻². After grinding, the electrodes were ultrasonically cleaned in ultrapure water for 30 min to remove any debris and then cycled potentiodynamically from -0.2 to 1.2 V at 50 mV s⁻¹ for 8 cycles in deoxygenated 0.5 mol L⁻¹ H₂SO₄. Well-defined features for Pt-oxide formation, Pt-oxide stripping, and hydrogen adsorption/desorption were typically observed after cycling.

Electrode Modification. To increase the electrochemically active area of the electrode and improve adhesion of the multienzyme film, $^{29,31-33}$ the Pt microelectrodes were potential cycled in a solution containing 2 mmol L^{-1} K_2PtCl_6 in 0.5 mol L^{-1} H_2SO_4 from -0.2 to 1.2 V at 10 mV s⁻¹ for 10 cycles with an initial potential of 1.0 V scanning cathodically to reduce Pt(IV) and initiate nanoparticle nucleation. This tactic was previously used to enhance the sensitivity and stability of ATP biosensors 52 and to platinize boron-doped diamond microelectrodes. 38 These electrodeposition conditions

produce a dispersed coverage of Pt nanoparticles across the substrate with a range of diameters. This is characteristic of a progressive nucleation and growth process in which new nuclei continuously form while existing Pt nanoparticles grow out of those nucleation sites. 53,54

To provide selectivity against potential oxidizable interferents, a permselective pmPD polymer film was electrodeposited onto the platinized-Pt microelectrode prior to enzyme immobilization. Using a deoxygenated 5 mmol L^{-1} mPD solution dissolved in 0.1 mol L^{-1} PB, pH 7.4, the potential was cycled from 0.2 to 1.0 V at 25 mV s⁻¹ for 40 cycles. In optimization experiments, the scan rate (10, 25, 50 mV s⁻¹) and cycle number (10, 20, 40) were optimized for sufficient H_2O_2 permeability and adequate rejection of electroactive interferents AA, DA, NE, and 5-HT.

Enzyme Immobilization. Following platinization and pmPD formation on the Pt microelectrodes, enzyme immobilization was performed by pipetting 1 μ L of a multienzyme solution containing equal volumes of 200 U mL⁻¹ ChOx, 400 U mL⁻¹ AChE, 10% (w/v) BSA to stabilize the enzymes, and 0.75% (v/v) glutaraldehyde onto the electrode surface under the aid of a low-power microscope. Enzyme immobilization is achieved through the cross-linking of the amino groups of the proteins in the enzyme layer using glutaraldehyde to form cross-linked aggregates that can impregnate the pores and channels of the pmPD support for enhanced stability. $^{20-24}$ The enzyme unit activity and solution concentration values were identical to those in the literature. 24 The electrodes were allowed to dry for 2 h at room temperature and were then immersed in 0.1 mol L⁻¹ phosphate buffer, pH 7.4, and stored in the fridge at 4 °C. The volume of multienzyme solution was optimized using 0.5, 1, 2, and 3 μ L.

Electrochemical and Surface Characterization. CV in 0.5 mol L-1 H2SO4 was used to determine the ECSA of the Pt microelectrodes before and after platinization. LSV was used to determine the oxidation potential of enzymatically produced H2O2 in response to increasing concentrations of ACh added to 10 mL of Krebs buffer, pH 7.4; these experiments helped determine the detection potential used for CA experiments, selecting an overpotential sufficient to drive the mass transport-limited oxidation of H₂O₂. CA was used to determine important figures of merit, including sensitivity, LOD, LOQ, linear dynamic range, reproducibility, sensor lifetime, and selectivity. Response curves were generated by plotting the current response to increasing concentrations of ACh added to 10 mL of magnetically stirred Krebs buffer, pH 7.4, with the electrode polarized at 0.75 V versus Ag/AgCl. Replicate measurements (n = 3) were used to assess reproducibility from sensor to sensor. SEM was used to evaluate the surface morphology of the modified Pt microelectrodes and to determine the microstructure of the pmPD films. Micrographs were taken using an ultra-high-resolution JEOL 7500F scanning electron microscope with a cold field emission emitter at the MSU Center for Advanced Microscopy. For non-conductive samples, a 30 s iridium sputter coating was used.

Ex Vivo Electrochemical Measurements. To account for any sensor-to-sensor variability, a calibration was performed in the flow bath used for Ex Vivo measurements by perfusing warm (36–37 $^{\circ}\text{C}$) Krebs buffer through a recording chamber at 4 mL min $^{-1}$ and recording the current response to increasing concentrations of ACh (0.1, 0.5, 1, 5, and 10 $\mu\text{mol L}^{-1}$) perfused through the chamber with the sensor polarized at 0.75 V versus Ag/AgCl. The average current just before the next calibration concentration was used to generate these calibration curves. These calibrations were performed once per day. In cases where two animals were tested within a single day, a second brief calibration was performed using only 1 $\mu\text{mol L}^{-1}$ ACh to verify the current response was unchanged.

For tissue preparation, a small (~1 cm) piece of the proximal-mid colon was removed from a euthanized mouse (48–54 weeks old); control mice were used only, and placed into a dish containing prewarmed (37 °C) Krebs buffer, pH 7.4. The fat and connective tissue were carefully removed, and the preparation was cut along the mesenteric border, stretched, and pinned flat using steel pins and fine forceps with the mucosa facing up. The mucosa and submucosa were carefully peeled back exposing the circular muscle, and a section of

this preparation (~0.5 cm²) was cut and transferred to a Sylgard-lined recording chamber using small (0.05 mm diam.) steel pins. The tissue was carefully stretched and pinned without tearing. A reference electrode (Ag/AgCl) and counter electrode (Pt wire) were secured opposite one another in the recording chamber. Warmed (36–37 °C) and oxygenated (95% O₂, 5% CO₂) Krebs buffer, pH 7.4, containing 1 μ mol L⁻¹ nifedipine (to block spontaneous muscle contractions) was perfused over the tissue at 4 mL min⁻¹ for 30 min to equilibrate the tissue. After 30 min, the calibrated ACh sensor was gently touched to a region of the tissue near a myenteric ganglion using a micromanipulator and low-power microscope. To position the microelectrode at "zero distance," the microelectrode was carefully touched to the tissue and backed off until the tissue was no longer contorted. The electrode was polarized at 0.75 V, and once the current stabilized, transmural electrical stimulation was accomplished by placing two Ag/AgCl wires on opposite ends of the tissue preparation. Voltage pulses were then delivered across these wires to stimulate all neurons and nerve fibers at 80 V, 10 Hz, and 0.5 ms pulse duration while increasing the number of voltage pulses delivered (10-50 pulses). The signal was also passed through a 60 Hz notch filter to remove line noise prior to digitization. As it is difficult to visualize the myenteric ganglia through the thickness of the circular muscle layer, a "test" stimulation was performed initially to determine if a sufficient response in the form of a current spike was achieved. If no response was observed, the electrode was moved until a "hotspot" rich with cholinergic neurons was located, as evidenced by a sharp and large current response after stimulation. Following electrical stimulation, the sodium channel blocker tetrodotoxin (TTX, 0.3 μ mol L⁻¹) was perfused over the tissue for 10 min before repeating stimulations to verify the neurogenic origin of the measured ACh release. After this, the tissue was rinsed for 20-30 min, and a single 50 pulse stimulation was repeated to verify the restoration of oxidation current. After this, the AChE inhibitor neostigmine (10 μ mol L⁻¹) was perfused for 10 min prior to repeating stimulations to examine the source of the measured oxidation current.

Statistical Analysis. Unless noted otherwise, data are presented as mean \pm SD for n=3 replicate measurements. Unpaired Student t-tests were used for comparing means between two groups. For ex vivo electrochemical measurements, oxidation currents were compared using a two-way ANOVA and Bonferroni's post hoc test to compare sample means using GraphPad Prism 9.5.1. To account for any potential sex differences, n=5 male and n=5 female mice were used.

ASSOCIATED CONTENT

Supporting Information

The Supporting Information is available free of charge at https://pubs.acs.org/doi/10.1021/acschemneuro.3c00337.

Optimization of the pmPD electrodeposition conditions and multi-enzyme layer; effect of platinization on biosensor response; scanning electron microscopy of the platinized-Pt microelectrode and pmPD films; and sensor lifetime and ex vivo electrochemical measurements (PDF)

AUTHOR INFORMATION

Corresponding Authors

James J. Galligan — Department of Pharmacology and Toxicology, Michigan State University, East Lansing, Michigan 48824, United States; Email: galliga1@msu.edu Greg M. Swain — Department of Chemistry, Michigan State University, East Lansing, Michigan 48824, United States; orcid.org/0000-0001-6498-8351; Email: swain@chemistry.msu.edu

Authors

Skye Henderson – Department of Chemistry, Michigan State University, East Lansing, Michigan 48824, United States Madison Strait – Department of Chemistry, Iowa State University, Ames, Iowa IA50011, United States

Roxanne Fernandes – Department of Pharmacology and Toxicology, Michigan State University, East Lansing, Michigan 48824, United States

Hui Xu – Department of Pharmacology and Toxicology, Michigan State University, East Lansing, Michigan 48824, United States

Complete contact information is available at: https://pubs.acs.org/10.1021/acschemneuro.3c00337

Author Contributions

The manuscript was written through the contributions of all authors. All authors have given approval to the final version of the manuscript. The design of the experiments was done by S.H., J.J.G., and G.M.S. S.H. and M.S. conducted the experiments and data analysis and contributed to the writing of the manuscript. Ex vivo electrochemical studies were performed by S.H. Animal handling and tissue preparation were performed by S.H., H.X., and R.F.

Notes

The authors declare no competing financial interest.

ACKNOWLEDGMENTS

Funding for the work was provided primarily through NIH R01 DK121272-01A1 (J.J.G. and G.M.S.) from the National Institutes of Health (USA). The research was performed with support from the National Science Foundation under grant no. CHE-2150173 (M.S. and G.M.S.). Any opinions, findings, conclusions, or recommendations expressed in this material are those of the author(s) and do not necessarily reflect the views of the National Science Foundation. The authors thank Ariana Miller from the University of Puerto Rico for her efforts early on in the project.

REFERENCES

- (1) DeTure, M. A.; Dickson, D. W. The Neuropathological Diagnosis of Alzheimer's Disease. *Mol. Neurodegener.* **2019**, *14*, 32.
- (2) Alzheimer's Association. 2023 Alzheimer's Disease Facts and Figures. Alzheimer's Dementia 2023, 19, 1598.
- (3) Terry, A. V., Jr.; Buccafusco, J. J. The Cholinergic Hypothesis of Age and Alzheimer's Disease-Related Cognitive Deficits: Recent Challenges and Their Implications for Novel Drug Development. J. Pharmacol. Exp. Ther. 2003, 306, 821–827.
- (4) H Ferreira-Vieira, T.; M Guimaraes, I.; R Silva, F.; M Ribeiro, F. Alzheimer's Disease: Targeting the Cholinergic System. *Curr. Neuropharmacol.* **2016**, *14*, 101–115.
- (5) Hampel, H.; Mesulam, M. M.; Cuello, A. C.; Farlow, M. R.; Giacobini, E.; Grossberg, G. T.; Khachaturian, A. S.; Vergallo, A.; Cavedo, E.; Snyder, P. J.; et al. The cholinergic system in the pathophysiology and treatment of Alzheimer's disease. *Brain* **2018**, 141, 1917–1933.
- (6) Bartus, R. T.; Dean, R. L.; Beer, B.; Lippa, A. S. The Cholinergic Hypothesis of Geriatric Memory Dysfunction. *Science* **1982**, *217*, 408–414
- (7) Contestabile, A. The History of the Cholinergic Hypothesis. *Behav. Brain Res.* **2011**, 221, 334–340.
- (8) Hasselmo, M. E. The Role of Acetylcholine in Learning and Memory. *Curr. Opin. Neurobiol.* **2006**, *16*, 710–715.
- (9) Drever, B. D.; Riedel, G.; Platt, B. The Cholinergic System and Hippocampal Plasticity. *Behav. Brain Res.* **2011**, 221, 505–514.
- (10) Maurer, S. V.; Williams, C. L. The Cholinergic System Modulates Memory and Hippocampal Plasticity via Its Interactions with Non-Neuronal Cells. *Front. Immunol.* **2017**, *8*, 1489.

- (11) Furness, J. B. Types of Neurons in the Enteric Nervous System. *J. Auton. Nerv. Syst.* **2000**, *81*, 87–96.
- (12) Han, X.; Tang, S.; Dong, L.; Song, L.; Dong, Y.; Wang, Y.; Du, Y. Loss of nitrergic and cholinergic neurons in the enteric nervous system of APP/PS1 transgenic mouse model. *Neurosci. Lett.* **2017**, 642, 59–65.
- (13) Pellegrini, C.; Daniele, S.; Antonioli, L.; Benvenuti, L.; D'Antongiovanni, V.; Piccarducci, R.; Pietrobono, D.; Citi, V.; Piragine, E.; Flori, L.; Ippolito, C.; Segnani, C.; Palazon-Riquelme, P.; Lopez-Castejon, G.; Martelli, A.; Colucci, R.; Bernardini, N.; Trincavelli, M. L.; Calderone, V.; Martini, C.; Blandizzi, C.; Fornai, M. Prodromal Intestinal Events in Alzheimer's Disease (AD): Colonic Dysmotility and Inflammation Are Associated with Enteric AD-Related Protein Deposition. *Int. J. Mol. Sci.* 2020, 21, 3523.
- (14) Stoye, N. M.; Santos Guilherme, M.; Endres, K. Alzheimer's Disease in the Gut—Major Changes in the Gut of 5xFAD Model Mice with ApoA1 as Potential Key Player. FASEB J. 2020, 34, 11883—11899.
- (15) Menden, A.; Hall, D.; Hahn-Townsend, C.; Broedlow, C. A.; Joshi, U.; Pearson, A.; Crawford, F.; Evans, J. E.; Klatt, N.; Crynen, S.; Mullan, M.; Ait-Ghezala, G. Exogenous lipase administration alters gut microbiota composition and ameliorates Alzheimer's disease-like pathology in APP/PS1 mice. *Sci. Rep.* **2022**, *12*, 4797.
- (16) Sun, Y.; Sommerville, N. R.; Liu, J. Y. H.; Ngan, M. P.; Poon, D.; Ponomarev, E. D.; Lu, Z.; Kung, J. S. C.; Rudd, J. A. Intra-Gastrointestinal Amyloid- β 1–42 Oligomers Perturb Enteric Function and Induce Alzheimer's Disease Pathology. *J. Physiol.* **2020**, 598, 4209–4223.
- (17) Johnson, C. D.; Barlow-Anacker, A. J.; Pierre, J. F.; Touw, K.; Erickson, C. S.; Furness, J. B.; Epstein, M. L.; Gosain, A. Deletion of Choline Acetyltransferase in Enteric Neurons Results in Postnatal Intestinal Dysmotility and Dysbiosis. *FASEB J.* **2018**, 32, 4744–4752.
- (18) Xin, Q.; Wightman, R. M. Enzyme modified amperometric sensors for choline and acetylcholine with tetrathiafulvalene tetracyanoquinodimethane as the electron-transfer mediator. *Anal. Chim. Acta* **1997**, 341, 43–51.
- (19) Aynacı, E.; Yasar, A.; Arslan, F. An amperometric biosensor for acetylcholine determination prepared from acetylcholinesterase-choline oxidase immobilized in polypyrrole-polyvinylsulpfonate film. *Sens. Actuators, B* **2014**, *202*, 1028–1036.
- (20) Barbosa, O.; Ortiz, C.; Berenguer-Murcia, A.; Torres, R.; Rodrigues, R. C.; Fernandez-Lafuente, R. Glutaraldehyde in Bio-Catalysts Design: A Useful Crosslinker and a Versatile Tool in Enzyme Immobilization. *RSC Adv.* **2014**, *4*, 1583–1600.
- (21) Sassolas, A.; Blum, L. J.; Leca-Bouvier, B. D. Immobilization Strategies to Develop Enzymatic Biosensors. *Biotechnol. Adv.* **2012**, 30, 489–511.
- (22) Nguyen, H. H.; Kim, M. An Overview of Techniques in Enzyme Immobilization. *Appl. Sci. Convergence Technol.* **2017**, *26*, 157–163.
- (23) Patel, B. A. Electrochemical Biosensors. In *Electrochemistry for Bioanalysis*; Patel, B., Ed.; Elsevier: Amsterdam, 2020; pp 267–284.
- (24) Mitchell, K. M. Acetylcholine and Choline Amperometric Enzyme Sensors Characterized in Vitro and in Vivo. *Anal. Chem.* **2004**, *76*, 1098–1106.
- (25) Bruno, J. P.; Gash, C.; Martin, B.; Zmarowski, A.; Pomerleau, F.; Burmeister, J.; Huettl, P.; Gerhardt, G. A. Second-By-Second Measurement of Acetylcholine Release in Prefrontal Cortex. *Eur. J. Neurosci.* **2006**, *24*, 2749–2757.
- (26) Burmeister, J. J.; Pomerleau, F.; Huettl, P.; Gash, C. R.; Werner, C. E.; Bruno, J. P.; Gerhardt, G. A. Ceramic-Based Multisite Microelectrode Arrays for Simultaneous Measures of Choline and Acetylcholine in CNS. *Biosens. Bioelectron.* **2008**, 23, 1382–1389.
- (27) Zhang, L.; Chen, J.; Wang, Y.; Yu, L.; Wang, J.; Peng, H.; Zhu, J. Improved Enzyme Immobilization for Enhanced Bioelectrocatalytic Activity of Choline Sensor and Acetylcholine Sensor. *Sens. Actuators, B* **2014**, *193*, 904–910.
- (28) Hou, S.; Ou, Z.; Chen, Q.; Wu, B. Amperometric acetylcholine biosensor based on self-assembly of gold nanoparticles and

- acetylcholinesterase on the sol-gel/multi-walled carbon nanotubes/choline oxidase composite-modified platinum electrode. *Biosens. Bioelectron.* **2012**, 33, 44–49.
- (29) Kucherenko, I. S.; Soldatkin, O. O.; Kucherenko, D. Y.; Soldatkina, O. V.; Dzyadevych, S. V. Advances in Nanomaterial Application in Enzyme-Based Electrochemical Biosensors: A Review. *Nanoscale Adv.* **2019**, *1*, 4560–4577.
- (30) Nunes, D.; Pimentel, A.; Gonçalves, A.; Pereira, S.; Branquinho, R.; Barquinha, P.; Fortunato, E.; Martins, R. Metal Oxide Nanostructures for Sensor Applications. *Semicond. Sci. Technol.* **2019**, *34*, 043001.
- (31) Kim, C. S.; Oh, S. M. Enzyme Sensors Prepared by Electrodeposition on Platinized Platinum Electrodes. *Electrochim. Acta* **1996**, *41*, 2433–2439.
- (32) De Corcuera, J. R.; Cavalieri, R. P.; Powers, J. R. Improved Platinization Conditions Produce a 60-Fold Increase in Sensitivity of Amperometric Biosensors Using Glucose Oxidase Immobilized in Poly-o-phenylenediamine. J. Electroanal. Chem. 2005, 575, 229–241.
- (33) Li, Y.; Sella, C.; Lemaître, F.; Guille Collignon, M.; Thouin, L.; Amatore, C. Highly Sensitive Platinum-Black Coated Platinum Electrodes for Electrochemical Detection of Hydrogen Peroxide and Nitrite in Microchannel. *Electroanalysis* **2013**, *25*, 895–902.
- (34) Killoran, S. J.; O'Neill, R. D. Characterization of Permselective Coatings Electrosynthesized on Pt—Ir From the Three Phenylenediamine Isomers for Biosensor Applications. *Electrochim. Acta* **2008**, *53*, 7303—7312.
- (35) Kucherenko, D. Y.; Siediuko, D. V.; Knyzhnykova, D. V.; Soldatkin, O. O.; Soldatkin, A. P. Development of Amperometric Biosensor for Choline Determination. *Biopolym. Cell* **2016**, 32, 229–234.
- (36) Murphy, L. J. Reduction of Interference Response at a Hydrogen Peroxide Detecting Electrode Using Electropolymerized Films of Substituted Naphthalenes. *Anal. Chem.* **1998**, *70*, 2928–2935.
- (37) Dai, Y. Q.; Zhou, D. M.; Shiu, K. Permeability and Permselectivity of Polyphenylenediamine Films Synthesized at a Palladium Disk Electrode. *Electrochim. Acta* **2006**, *52*, 297–303.
- (38) Henderson, S.; Bhardwaj, K.; Perugachi, V.; Espinoza-Montero, P.; Galligan, J. J.; Swain, G. M. *In Vitro* Monitoring of Nitric Oxide Release in the Mouse Colon Using a Boron-Doped Diamond Microelectrode Modified with Platinum Nanoparticles and Nafion. *Anal. Chem.* **2022**, *95*, 1027–1037.
- (39) Raves, M. L.; Giles, G.; Schrag, J. D.; Schmid, M. F.; Phillips, G. N., Jr.; Chiu, W.; Howard, A. J.; Silman, I.; Sussman, J. L. Quaternary Structure of Tetrameric Acetylcholinesterase. In *Structure and Function of Cholinesterases and Related Proteins*; Springer, 1998; pp 351–356.
- (40) Quaye, O.; Lountos, G. T.; Fan, A. M. O.; Orville, A. M.; Gadda, G. Role of Glu312 in Binding and Positioning of the Substrate for the Hydride Transfer Reaction in Choline Oxidase. *Biochem* **2008**, 47, 243–256
- (41) Kennedy, B.; Glidle, A.; Cunnane, V. J. A Study of the Oxidation and Polymerisation of Meta Substituted Phenol and Aniline Derivatives. *J. Electroanal. Chem.* **2007**, *608*, 22–30.
- (42) Zhou, H.; Chen, H.; Luo, S.; Chen, J.; Wei, W.; Kuang, Y. Preparation and Bioelectrochemical Responses of the Poly(*m*-Phenylenediamine) Glucose Oxidase Electrode. *Sens. Actuators, B* **2004**, *101*, 224–230.
- (43) Johnston, D. A.; Cardosi, M. F.; Vaughan, D. H. The electrochemistry of hydrogen peroxide on evaporated gold/palladium composite electrodes. Manufacture and electrochemical characterization. *Electroanalysis* **1995**, *7*, 520–526.
- (44) Hall, S. B.; Khudaish, E. A.; Hart, A. L. Electrochemical Oxidation of Hydrogen Peroxide at Platinum Electrodes. Part 1. An Adsorption-Controlled Mechanism. *Electrochim. Acta* **1998**, 43, 579–588.
- (45) Stevens, C. F.; Wesseling, J. F. Activity-Dependent Modulation of the Rate at which Synaptic Vesicles Become Available to Undergo Exocytosis. *Neuron* **1998**, *21*, 415–424.

- (46) Harrington, A. M.; Hutson, J. M.; Southwell, B. R. Cholinergic Neurotransmission and Muscarinic Receptors in the Enteric Nervous System. *Prog. Histochem. Cytochem.* **2010**, *44*, 173–202.
- (47) Uutela, P.; Reinilä, R.; Piepponen, P.; Ketola, R. A.; Kostiainen, R. Analysis of Acetylcholine and Choline in Microdialysis Samples by Liquid Chromatography/Tandem Mass Spectrometry. *Rapid Commun. Mass Spectrom.* **2005**, *19*, 2950–2956.
- (48) Nirogi, R.; Mudigonda, K.; Kandikere, V.; Ponnamaneni, R. Quantification of Acetylcholine, an Essential Neurotransmitter, in Brain Microdialysis Samples by Liquid Chromatography Mass Spectrometry. *Biomed. Chromatogr.* **2010**, *24*, 39–48.
- (49) Asri, R.; O'Neill, B.; Patel, J. C.; Siletti, K. A.; Rice, M. E. Detection of evoked acetylcholine release in mouse brain slices. *Analyst* **2016**, *141*, 6416–6421.
- (50) Scimemi, A.; Beato, M. Determining the Neurotransmitter Concentration Profile at Active Synapses. *Mol. Neurobiol.* **2009**, *40*, 289–306.
- (51) Köppen, A.; Klein, J.; Schmidt, B. H.; Ver Der Staay, F.-J.; Löffelholz, K. Effects of Nicotinamide on Central Cholinergic Transmission and on Spatial Learning in Rats. *Pharmacol. Biochem. Behav.* **1996**, *53*, 783–790.
- (52) Peteu, S. F.; Russell, S. A.; Galligan, J. J.; Swain, G. M. An Electrochemical ATP Biosensor with Enzymes Entrapped within a PEDOT Film. *Electroanalysis* **2021**, *33*, 495–505.
- (53) Bennett, J. A.; Show, Y.; Wang, S.; Swain, G. M. Pulsed Galvanostatic Deposition of Pt Particles on Microcrystalline and Nanocrystalline Diamond Thin-Film Electrodes: I. Characterization of As-Deposited Metal/Diamond Surfaces. *J. Electrochem. Soc.* **2005**, 152, No. E184.
- (54) Bennett, J. A.; Swain, G. M. Investigating the Nucleation and Growth of Electrodeposited Pt on Polycrystalline Diamond Electrodes. *J. Electrochem. Soc.* **2010**, *157*, F89–F95.

☐ Recommended by ACS

Three-Dimensional Cardiomyocyte-Nanobiosensing System for Specific Recognition of Drug Subgroups

Kai Zhu, Ning Hu, et al.

JUNE 11, 2023 ACS SENSORS

READ 🗹

Recent Advances in the Development and Characterization of Electrochemical and Electrical Biosensors for Small Molecule Neurotransmitters

Jiayi He, Christy L. Haynes, et al.

MARCH 20, 2023

ACS SENSORS

READ 🗹

Microelectrode-Based Electrochemical Impedance Determination of Brain-Derived Neurotrophic Factor in Aqueous Humor for Diagnosis of Glaucoma

Xin Xie, Guokun Liu, et al.

JANUARY 11, 2023

ANALYTICAL CHEMISTRY

READ 🗹

Monitoring the Activity and Inhibition of Cholinesterase Enzymes using Single-Walled Carbon Nanotube Fluorescent Sensors

Dan Loewenthal, Gili Bisker, et al.

OCTOBER 07, 2022

ANALYTICAL CHEMISTRY

READ 🗹

Get More Suggestions >